Modeling and Analysis of Spoke-Type Permanent Magnet Vernier Machine Based on Equivalent Magnetic Network Method

Shan Jiang[1,2], *Guohai Liu*[1,2], *Wenxiang Zhao*[1,2]*, *Liang Xu*[1,2], *and Qian Chen*[1,2]

(1. School of Electrical and Information Engineering, Jiangsu University, Zhenjiang 212013, China;

2. Jiangsu Key Laboratory of Drive and Intelligent Control for Electric Vehicle, Zhenjiang 212013, China)

Abstract: In this paper, a new equivalent magnetic network(EMN) model is established for a spoke-type permanent magnet(PM) vernier(PMV) machine. Two different modeling methods are proposed for different parts of the PMV machine, considering that their magnetic field distributions are quite different. Hierarchical modeling method is proposed for the modeling of the rotor as the magnetic intensity of the rotor iron core presents gradient distribution along the radial direction. Mesh based reluctance network method is used for the modeling of flux modulation poles with irregular and unstable magnetic field distributions. Moreover, accurate PM leakage permeance calculation formulae are deduced to improve the simulation precision. The electromagnetic parameters, such as flux linkage, back electromagnetic force, electromagnetic torque and iron loss are predicted by the proposed EMN model. Finally, finite element analysis(FEA) and experimental results are given to verify the effectiveness of the proposed methods.

Keywords: Equivalent magnetic network(EMN), permanent magnet vernier(PMV) machine, hierarchical modeling method, mesh based reluctance network, finite element analysis(FEA).

1 Introduction

Permanent magnet(PM) vernier(PMV) machines have received increasing attention in wind power generation and direct-drive applications due to their inherently low speed and high torque characteristics [1-4]. In order to further improve performance, a hybrid stator fault-tolerant(FT) PMV(FTPMV) machine was proposed in [5]. By adopting the new stator and spoke-type PMs, the performance of torque density, power factor and efficiency were improved. However, due to the multi-pole and spoke-type arrangement of the PMs, this machine suffers from serious PM flux leakage, tooth-tip flux leakage and complex flux distribution in flux-modulation poles (FMPs), which greatly increases the modeling difficulty of equivalent magnetic network (EMN) methodology.

The PM flux leakage and tooth-tip flux leakage have significant influence on the simulation accuracy of the EMN model[6-12], but relevant research about PMV machines is limited[13-14]. In [13], an EMN model for a surface-mounted PMV machine was established to analyze the tooth-tip flux leakage. However, iron core saturation was ignored and the model can only be applied to no-load condition. In [14], a novel calculation method for air-gap permeance and tooth tip permeance was proposed. As this method cannot be applied to on-load condition and no-load condition at the same time, separate EMN models were built for the two working conditions, indicating that the modeling solutions for PMV machine were not mature enough. However, the EMN models of salient pole machine and spoke-type PM machine can be used as a reference, as the two types of machines and the spoke-type FTPMV machine have similar topology. In [6], EMN models were built for a mutually coupled linear switched reluctance machine and a surface mounted linear PM machine, in which piecewise linearization method was adopted to calculate the air-gap permeance by introducing overlapping coefficient of translator teeth and stator teeth. In [15] and [16], the machines have large slot opening width, and the magnetic lines in air gap region are scattering, thereby, the effective length and cross-sectional area of air-gap permeance will change with position. The air-gap regions were then divided into many segments to accurately calculate the effective lengths of flux paths so as to obtain higher accuracy. The modeling of pole shoe is also a key point, because the uneven flux distribution in pole shoe area may lead to local iron saturation[17-18]. The impact of local magnetic saturation on simulation accuracy was studied in [17], where results show that the errors under various areas of saturation regions were changed from −5% to 5%. In [18], a fitting method was used to model the saturation distribution on poles. By integrating the variables of geometry and rotor position, the fitting data was dependent on the pole pair position and phase current, making the calculation of flux linkage characteristics simpler and more accurate. As well, an EMN model for a spoke-type PM machine was investigated in [19], in which the modeling method for spoke-type PM and air-gap were introduced. However, the PM end leakage was omitted, even though this issue

*Corresponding Author, Email: zwx@ujs.edu.cn.

Supported by National Natural Science Foundation of China under Grant 51577084, Key Project of Natural Science Foundation of Jiangsu Higher Education Institutions under Grant 15KJA470002, and the Priority Academic Program Development of Jiangsu Higher Education Institutions.

was an important topic in improving simulation precision.

For the spoke-type FTPMV machine, the flux density distribution of rotor iron core is uneven, which leads to different degrees of magnetic saturation. Additionally, the PM end leakage has a more significant effect on simulation precision. These issues are specific to the spoke-type FTPMV machine and the purpose of this paper is to solve such difficulties. Many different modeling methods are proposed for different parts of the FTPMV machine to better account for magnetic saturation, flux leakage and complex magnetic field distribution. An EMN model is built for this machine, and can be used for optimal design and performance prediction. In Section 2, the topology and design parameters of the FTPMV machine are briefly introduced. The modeling details are then presented in Section 3 and the solution process is given in Section 4. In Section 5, simulation results are given to make a comparison with that of finite element(FE) analysis(FEA) and experimental tests. Finally, conclusions are drawn in Section 6.

2 Machine specifications

The cross-sectional topology and photograph of the spoke-type FTPMV machine are shown in Fig.1(a) and Fig.1(b), respectively. The spoke-array PMs with flux concentration are inlaid in the rotor iron core. The armature teeth and FT teeth are alternately distributed in the circumferential direction, and the FMPs are formed by both the straight teeth and split-teeth. Single-layer concentrated winding design is adopted to reduce electromagnetic coupling of phases. The design parameters are listed in Table 1.

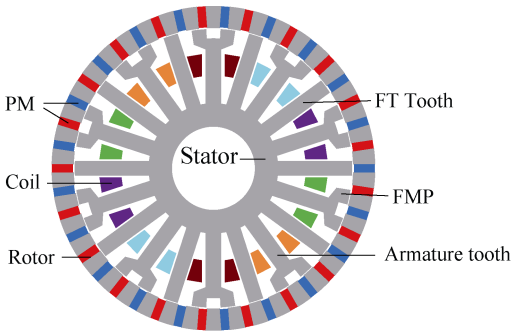

(a) Cross-sectional topology

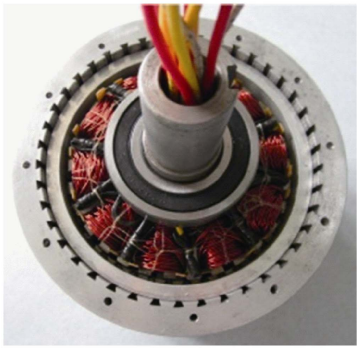

(b) Photograph

Fig.1 Spoke-type FTPMV machine

Table 1 Design parameters of the spoke-type FTPMV machine

Parameters	Values
Phases	5
Rated speed /(r/min)	600
Rated voltage /V	60
Rated current /A	10
Number of slots	20
Number of rotor pole-pairs	21
Outside rotor radius/mm	70
Inside rotor radius/mm	60.5
Outside stator radius/mm	60
Stack length/mm	60
Air-gap width/mm	0.5
FMP width/mm	6.28
PM width/mm	3.5
Stator tooth width/mm	6.63
Turns per phase/mm	100
Remanence of PM/T	1.23
Iron core lamination	50WW465

Fig.2(a) and Fig.2(b) show the magnetic field distributions of the spoke-type FTPMV machine when the rotor position (θ) are 0° and 90° (electrical angle), respectively. It can be seen that the flux distributions in air-gap and FMPs are irregular and complex, and will be influenced by rotor position and armature magnetomotive force. It seems that the flux line distribution of the spoke-type FTPMV machine is similar to that of the PMV machine proposed in [14], but the rotor flux distributions of the two machines have great differences. In addition, the PM end leakage in the spoke-array FTPMV machine is more sensitive to the main flux. It is necessary to establish accurate models for rotor and PM end leakage, and the main contribution of this paper is to propose corresponding solutions for these issues.

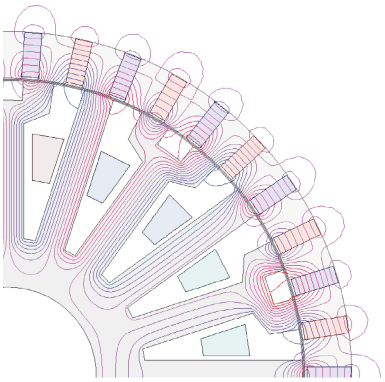

(a) θ=0° (electrical angle)

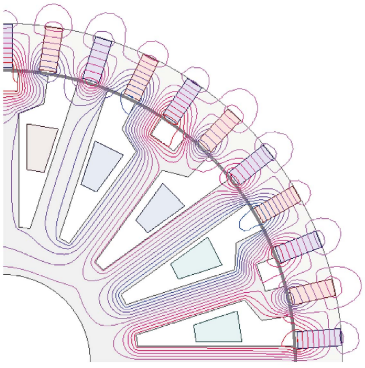

(b) θ=90° (electrical angle)

Fig.2 Magnetic flux distributions of the spoke-type FTPMV machine at different rotor positions

3 Modeling process

3.1 Rotor

Since the magnetic lines in the boundary region of PMs will form leakage circuits, the rotor iron core cannot be simply considered as a magnetic equipotential body. As shown in Fig.3, the magnetic intensity of the rotor iron presents gradient distribution along the radial direction. For simplicity, the PMs and the rotor iron core are divided into four layers along the radial direction, and the equivalent EMN model can thus be built as shown in Fig.4, where G_{air} is the external air gap leakage permeance, G_{pm} and G_{iron} are the permeances of PM and iron core, respectively. The region shape of G_{air} is a semi annular, where its calculation formula can be expressed as:

$$G_{\text{air}} = \int_{r_1}^{r_2} \frac{\mu_0 L_{\text{d}}}{\pi x} \mathrm{d}x = \frac{\mu_0 L_{\text{d}}}{\pi} \ln \frac{r_2}{r_1} \tag{1}$$

where L_{d} is the stack length, r_1, r_2 are the inner radius and outer radius of the semi annular, respectively. The region shapes of G_{pm} and G_{iron} are regular rectangle, and their values can be obtained by a unified mathematical expression:

$$G = \frac{\mu_0 \mu_{\text{r}} S}{L} \tag{2}$$

where G represents permeance, μ_0 is vacuum permeability, μ_{r} is relative permeability, S and L are the effective sectional area and the effective length, respectively. Besides, the magnetomotive force of the spoke-type PM (F_{pm}) can be expressed as:

$$F_{\text{pm}} = H_{\text{c}} l_{\text{pm}} \tag{3}$$

where H_{c} and l_{pm} are the magnetic field intensity and excitation length of PM.

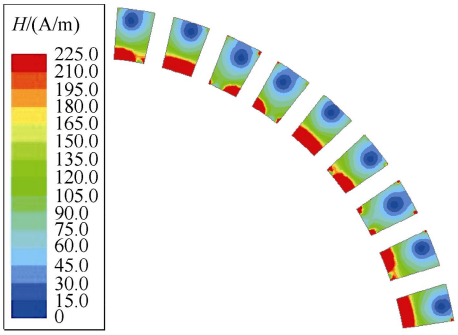

Fig.3 Magnetic intensity distribution nephogram of the rotor iron core

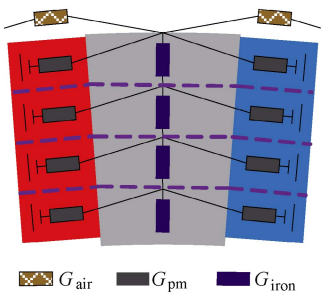

Fig.4 EMN model of rotor

3.2 Stator

The stator yokes, FT teeth and armature teeth are regular-shaped and the flux distributions of these regions are regular. Hence, their permeances can be calculated using (2). However, as the flux distributions in FMPs are irregular and unstable, they are hard to model using traditional magnetic circuit methods. As discussed in [20], using a mesh-based reluctance network taking the circumferential and radial branches into account, is an effective way to simulate the magnetic field distribution with different flux flow directions. This method can be employed for the modeling of FMPs. In Fig.5, the FMP is divided into four parts. G_x and G_y are the permeance components in the circumferential direction and the radial direction, respectively, and they can be calculated by

$$\begin{cases} G_x = \dfrac{2\mu_0 \mu_{\text{r}} L_{\text{d}} b}{a} \\ G_y = \dfrac{2\mu_0 \mu_{\text{r}} L_{\text{d}} a}{b} \end{cases} \tag{4}$$

where a and b are the length and width of the FMP, respectively. The magnetomotive force of winding follows the current low, in which the displacement current is neglected and only the conduction current is considered. Hence the winding magnetomotive force(F_{w}) can be denoted as:

$$F_{\text{w}} = N_{\text{c}} i \tag{5}$$

where N_{c} and i are the winding turns per coil and current, respectively.

The EMN model of stator is established as shown in Fig.6, where G_{sy}, G_{at}, G_{ft}, G_{ps}, and G_{fmp} are the permeances of stator yoke, armature tooth, FT tooth, armature tooth pole shoe and FMP, respectively.

3.3 Air-gap

According to the magnetic field boundary condition and minimum reluctance principle, the regions of air-gap permeances are rectangular and fan-shaped. These rectangular air-gap permeances should be calculated by (2), and these fan-shaped ones as shown in Fig.7 can be calculated by:

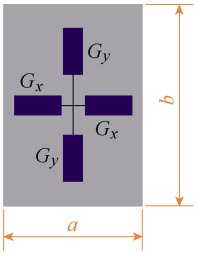

Fig.5 Mesh-based reluctance network

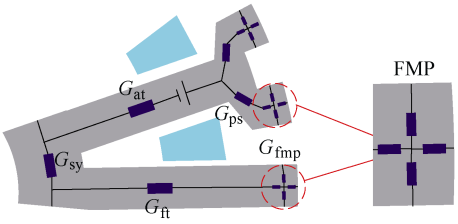

Fig.6 EMN model of stator

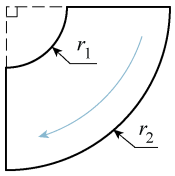

Fig.7 Fan-shaped air-gap region

$$G=\frac{2\mu_0 L_d}{\pi}\ln\frac{r_2}{r_1} \tag{6}$$

where r_1 and r_2 are the inside and outside radius of the fan-shaped region, respectively.

Taking into account the PM flux leakage in the air-gap region, there are three relative positions between the rotor PM and FMP, namely the non-overlapping, the partial overlapping and the exact overlapping, corresponding to Fig.8(a)~Fig.8(c). The PM leakage flux paths of the three cases are depicted by blue lines with arrows.

In Fig.8(a), the flux paths are a series of arcs with differing radius. The corresponding region shape can be regarded as an isosceles triangle (the base length and height are w_{pm} and w_{g1}, respectively), and the effective length of flux path is approximately equal to the length of waist line. Letting G_{nl1} be the permeance of the area where the red line frame located, its calculation can be written as:

$$\begin{aligned}G_{nl1}&=\int_0^{w_{g1}}\frac{\mu_0 L_d}{\sqrt{(w_{pm}/2)^2+x^2}}\mathrm{d}x\\&=\mu_0 L_d\ln\left(\frac{w_{g1}+\sqrt{(w_{pm}/2)^2+w_{g1}^2}}{w_{pm}/2}\right)\end{aligned} \tag{7}$$

where w_{pm} is the width of PM, w_{g1} is the distance between PM and stator. The flux leakage permeance of the this case (G_{nl}) can hence be denoted by:

$$G_{nl}=0.5G_{nl1} \tag{8}$$

In Fig.8(b), the leakage permeance (G_{pl}) consists two parts: G_{pl1} and G_{pl2}, and their regions are marked with red wireframe. G_{pl1} and G_{pl2} are calculated by:

$$G_{pl1}=\int_0^{x_{pl}}\frac{\mu_0 L_d}{\sqrt{x_{pl}^2+x^2}}\mathrm{d}x=0.88\mu_0 L_d \tag{9}$$

$$G_{pl2}=\begin{cases}\dfrac{2\mu_0 L_d}{\pi}\ln\dfrac{w_{g1}}{w_g}, & \text{if } w_{pm}-x_{pl}>w_{g1}\\ \dfrac{2\mu_0 L_d}{\pi}\ln\dfrac{w_{pm}-x_{pl}}{w_g}, & \text{if } w_{g1}>w_{pm}-x_{pl}>w_g\\ G_{nl}, & \text{others}\end{cases} \tag{10}$$

where x_{pl} is the non-overlapping length of PM and FMP, w_g is air-gap width. Then G_{pl} can be gained by:

$$G_{pl}=\frac{G_{pl1}\cdot G_{pl2}}{G_{pl1}+G_{pl2}} \tag{11}$$

In Fig.8(c), the flux lines will flow through the FMP along the tangential direction, however, the magnetic potential drop can be neglected. Then the permeance of PM leakage flux (G_{ol}) can be written as (12).

$$\begin{aligned}G_{ol}&=0.5G_{ol1}\\&=0.5\left[\int_0^{w_g}\frac{\mu_0 L_d}{\sqrt{w_g^2+x^2}}\mathrm{d}x+\mu_0 L_d\ln\frac{w_{g1}}{w_g}+\frac{\mu_0 L_d(0.5w_{pm}-w_{g1})}{\frac{\pi}{2}w_{g1}}\right]\\&=0.5\mu_0 L_d\left[0.88+\ln\frac{w_{g1}}{w_g}+\frac{w_{pm}-2w_{g1}}{\pi w_{g1}}\right]\end{aligned} \tag{12}$$

Finally, the complete EMN model for the spoke-type FTPMV machine is built as shown in Fig.9.

4 Solution process

The solution process contains the following steps:

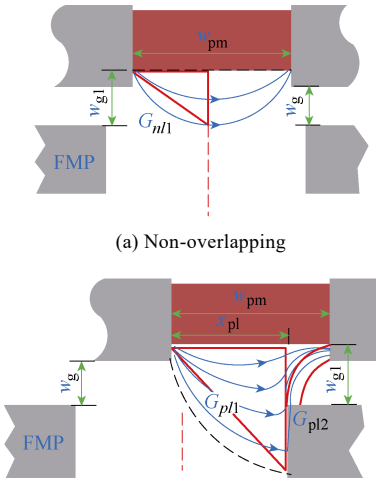

(a) Non-overlapping

(b) Partial overlapping

(c) Exact overlapping

Fig.8 Relative positions between PM and FMP

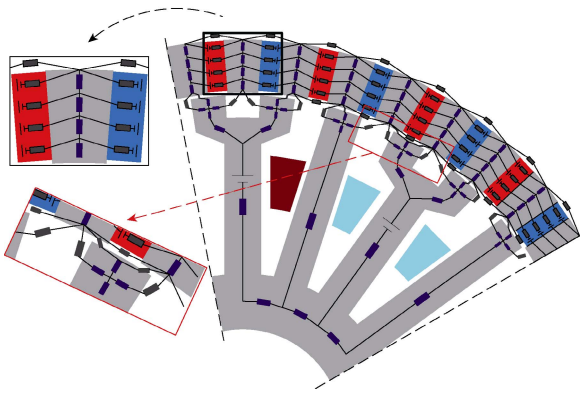

Fig.9 EMN model of the spoke-type FTPMV machine

Step 1: Set the initial position of rotor, simulation cycle and simulation step size.

Step 2: Calculate all of the permeances and magnetomotive forces, then establish nodal current equations.

The initial permeability should be first obtained to initialize the nonlinear permeances, and can be set as:

$$\mu_{\text{ini}} = \frac{B_{BH}(2) - B_{BH}(1)}{H_{BH}(2) - H_{BH}(1)} \tag{13}$$

where μ_{ini} is the initial permeability, ($H_{BH}(1)$, $B_{BH}(1)$) and ($H_{BH}(2)$, $B_{BH}(2)$) are the first point and the second point of the *B-H* curve. Meanwhile, the nodal current equations in matrix form can be listed using Kirchhoff's current law:

$$\begin{bmatrix} G(1,1) & \cdots & G(1,n) \\ \vdots & \vdots & \vdots \\ G(n,1) & \cdots & G(n,n) \end{bmatrix} \begin{bmatrix} F(1) \\ \vdots \\ F(n) \end{bmatrix} = \begin{bmatrix} \Phi(1) \\ \vdots \\ \Phi(n) \end{bmatrix} \tag{14}$$

It can be abbreviated as:

$$\boldsymbol{G} \cdot \boldsymbol{F} = \boldsymbol{\Phi} \tag{15}$$

where $\boldsymbol{G}$, $\boldsymbol{F}$ and $\boldsymbol{\Phi}$ are the permeance matrix, nodal potential matrix and flux matrix, respectively.

Step 3: Solve nodal current equations.

In (15), $\boldsymbol{F}$ is the unknown variable, and can be solved using Matlab code:

$$\boldsymbol{F} = \text{inv}(\boldsymbol{G}) \cdot \boldsymbol{\Phi} \quad \text{or} \quad \boldsymbol{F} = \boldsymbol{G} \backslash \boldsymbol{\Phi} \tag{16}$$

The flux linkage (Φ) and flux density (B) can be calculated by:

$$\begin{cases} \boldsymbol{\Phi} = (\boldsymbol{F}(i) - \boldsymbol{F}(j)) \times \boldsymbol{G}(i,j) \\ B = \dfrac{\boldsymbol{\Phi}}{S} \end{cases} \tag{17}$$

where i and j are the node numbers of the both ends of a permeance, S is the cross-sectional area where $\boldsymbol{\Phi}$ pass through.

Step 4: Update the permeability of nonlinear material.

The permeability of nonlinear material should be updated by searching *B-H* curve:

$$\begin{cases} H = H_{BH}(k) + \dfrac{(H_{BH}(k+1) - H_{BH}(k))(B - B_{BH}(k))}{B_{BH}(k+1) - B_{BH}(k)} \\ \mu_{\text{new}} = \dfrac{B}{H} \end{cases} \tag{18}$$

where μ_{new} is the updated permeability. In order to enhance iterative convergence, the newly obtained permeability should be reset using a correction factor:

$$\mu^{(k)} = f_{\text{c}} \mu_{\text{new}} + (1 - f_{\text{c}}) \mu^{(k-1)} \tag{19}$$

where k represents iteration number, f_{c} is the correction factor ($0 < f_{\text{c}} < 1$) and it's optimum value is 0.31.

Step 5: Update nodal current equations until the error requirement is met.

The $\mu^{(k)}$ obtained in step 4 will be used to rebuilt the nodal current equations listed as (14), and the iterative process can be finalized when the following criterion is satisfied.

$$\left| \mu^{(k)} - \mu^{(k-1)} \right| < \zeta \tag{20}$$

where ζ is the error tolerance, it's value can be set as 1.0e-5.

Step 6: Change rotor position to obtain the complete simulation waveform of an electrical cycle.

The corresponding flowchart of the process is drawn in Fig.10.

5 Results validation

In order to validate the effectiveness of the proposed model, a two dimension FE model was built and experimental tests were carried out. The comparison results are given as follow.

5.1 Flux linkage and electromotive force

The flux linkages of every phase can be acquired by (17), and the back electromotive forces (back-EMFs) can be obtained by:

$$E = -N_{\text{c}} \frac{\text{d}\Phi_{\text{ph}}}{\text{d}t} \tag{21}$$

where E is the back-EMF, N_{c} is the number of turns per coil, and Φ_{ph} is the flux linkage of armature tooth.

The no-load flux linkage and back-EMF of phase A obtained by EMN model, FE model and experimental test are compared in Fig.11. The flux linkage amplitudes of EMN result and FE result are 51.79mWb and 51.71mWb, respectively (the error is less than 2%). The back-EMF amplitudes of EMN method, FEA and test

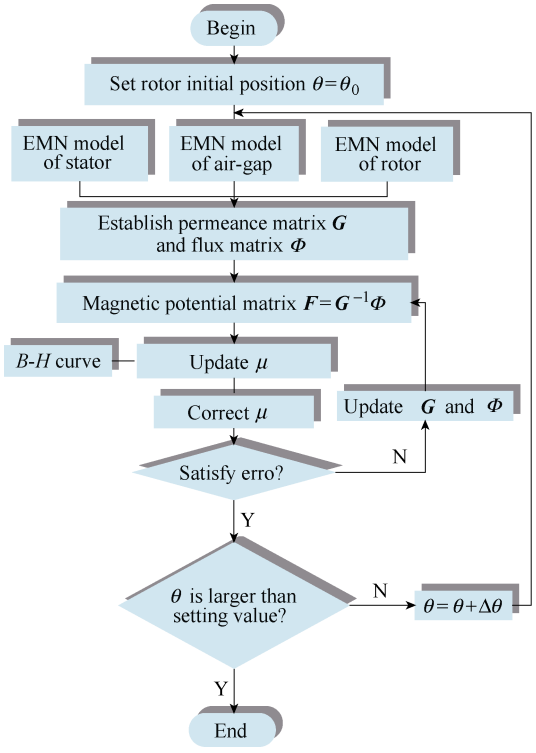

Fig.10 Flowchart of solution process

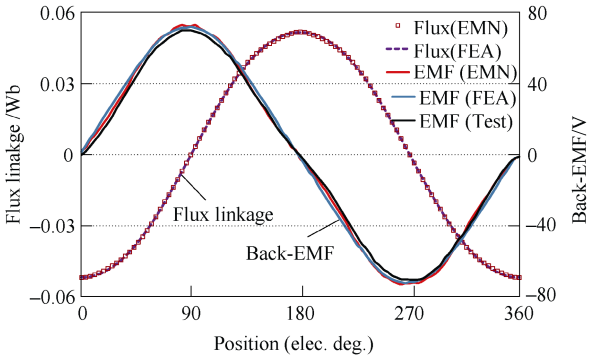

Fig.11 Comparison of flux linkage and back-EMF

are 72.0V, 71.5V and 70.0V, respectively. Meanwhile, harmonic content of back-EMF waveforms are analyzed in Fig.12. The content of the third harmonics have obvious errors, which is mainly caused by the machining error of prototype and the modeling error of the EMN model. However, it is found from Fig.12 that the magnitudes of the 3rd harmonics are far less than that of fundamental waves, and the errors in 3rd harmonic content do not significantly affect the main waveforms. Generally, the results are in good agreement with each other, which confirms the accuracy of the proposed model.

In addition, Fig.13 studies the effect of PM leakage permeance on main flux linkage. The amplitude error of the two waveforms is as high as 15%, hence, it is necessary to take PM end leakage into consideration for the spoke-type FTPMV machine. Moreover, flux linkage versus PM thickness is compared in Fig.14, it is seen that the increase rate of flux linkage becomes slow when the PM thickness is more than 3.5mm. The results of EMN method and FEA show slight deviation when the PM thickness is less than 3mm, which is caused by the simplification of the PM leakage circuits

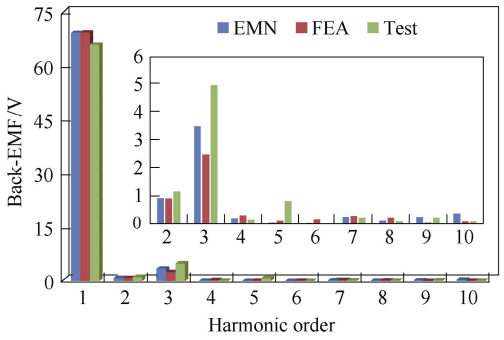

Fig.12 Harmonic analysis of back-EMF

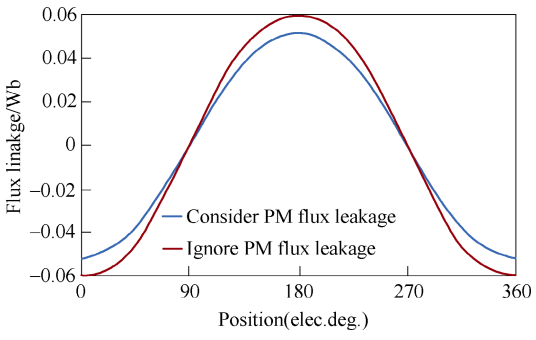

Fig.13 Effect of PM flux leakage on main flux

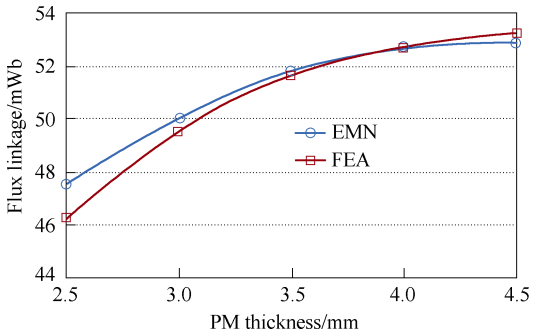

Fig.14 Flux linkage amplitude versus PM thickness

5.2 Air-gap flux density

The air-gap flux density (B_{air}) can be obtained by:

$$B_{air} = \frac{\Delta F \times G}{S} = \frac{\mu_0 \Delta F}{l} \tag{22}$$

where ΔF and l are the magnetic potential drop and the effective length of air-gap flux lines. Hence, as shown in Fig.15, the air-gap flux density of position ① and position ② should be calculated by (23) and (24), respectively.

$$B_{air1} = \frac{\mu_0 \left(F_k - F_m\right)}{L_1} \tag{23}$$

$$B_{air2} = \frac{\mu_0 \left(F_k - F_n\right)}{L_2} \tag{24}$$

where F_k, F_m and F_n are nodal magnetic potentials, L_1 and L_2 are the effective lengths of the air-gap flux lines in position ① and position ②, respectively. The air-gap flux densities in other positions can also be obtained using the same method, and the simulation results of EMN model and FE model are compared in Fig.16. It can be seen that the waveforms in Fig.16 have very good agreement with each other.

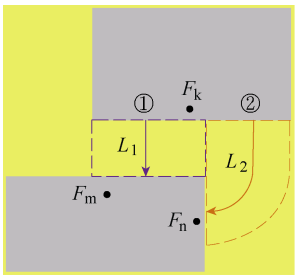

Fig.15 Calculation of air gap flux density

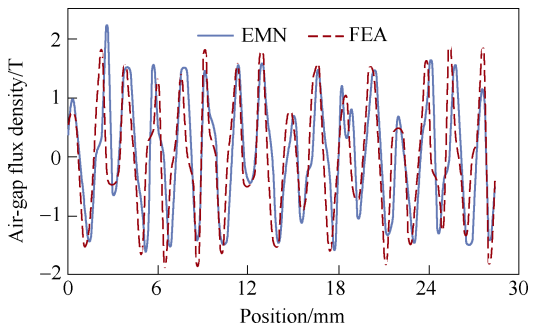

Fig.16 Air-gap flux density

5.3 Electromagnetic torque

The electromagnetic torque (T) is calculated by:

$$T = \frac{5}{2}\frac{U_{pv}I_{pv}\cos\theta}{\Omega} \tag{25}$$

where U_{pv} and I_{pv} are the peak value of back-EMF and current, respectively. θ is internal active power angle and Ω is the mechanical angular velocity of rotor. The simulation results of EMN model and FE model are compared with the experimental test (the current is 2.6A, rotor speed is 238r/min), as shown in Fig.17. The torque ripple of the test result is caused by cogging torque and mechanical friction, however, these issues do not have significant influence on the electromagnetic torque component. The mean values of the waveforms are 6.96N·m(EMN), 7.12N·m(FEA) and 7.07N·m(Test), respectively, the errors are less than 1.6%. Fig.18 shows the current-torque characteristic of the FTPMV machine, indicating the error between EMN result and FEA result is less than 5.7%.

5.4 Iron loss

Finally, iron loss is predicted using the discrete calculation method[20]:

$$P_{Fe} = k_h fB^2 + k_c (fB)^2 + k_e (fB)^{1.5} \tag{26}$$

where P_{Fe} represents iron loss, f is frequency and B is flux density. k_h, k_c and k_e are the coefficients of hysteresis loss, eddy current loss and excess loss, respectively. The calculation results of iron loss versus current are compared in Fig.19. It is observed that the increasing tendencies of iron loss with current show good agreement, and the calculation error between EMN method and FEA is less than 7.7%, which further confirms the accuracy of the proposed model.

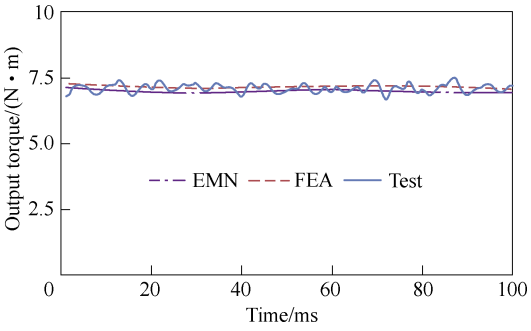

Fig.17 Electromagnetic torque

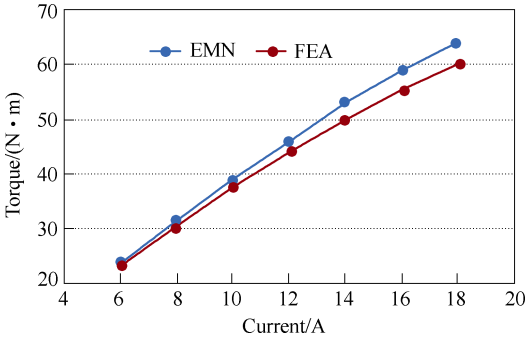

Fig.18 Electromagnetic torque versus current

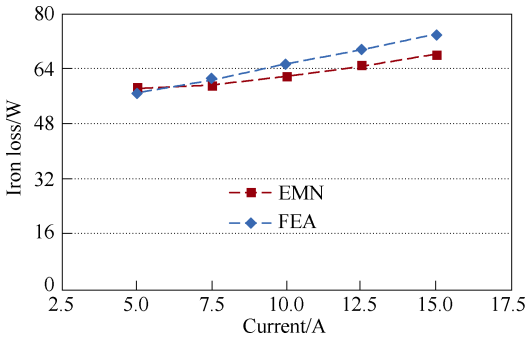

Fig.19 Iron loss versus current

6 Conclusion

In this paper, a nonlinear EMN model is proposed for the performance analysis of a spoke-type FTPMV machine, in which a hierarchical modeling method and mesh-based reluctance network are employed for the modeling of rotor and FMPs, taking unequal magnetic potential distribution and complex flux distribution into account. PM flux leakage is also considered and the corresponding permeance calculations are deduced. Simulation results show that the proposed model has very high precision. Compared with FE model, the time requirement for the solution process of the EMN model is greatly reduced by approximately a factor of 24 (the EMN model only takes 5 minutes while the FE model takes about 2 hours), hence the EMN method presents great superiority in computational efficiency.

References

[1] K. Xie, D. Li, R. Qu, and Y. Gao, "A novel permanent magnet vernier machine with halbach array magnets in stator slot opening," *IEEE Trans. Magn.*, vol. 53, no. 6, pp.1-5, Art. ID. 7207005, Jan. 2017.

[2] D. Jang and J. Chang, "Effects of flux modulation poles on the radial magnetic forces in surface-mounted permanent-magnet vernier machines," *IEEE Trans. Magn.*, vol. PP, no. 99, Art. ID. 8202704, Feb. 2017.

[3] W. Li, T. W. Ching, and K. T. Chau, "A new high-temperature superconducting vernier permanent-magnet machine for wind turbines," *IEEE Trans. Appl. Supercond.*, vol. 27, no. 4, pp.1-5, Art. ID. 5202905, Jun. 2017.

[4] Y. Oner, Z. Q. Zhu, L. J. Wu, X. Ge, H. Zhan, and J. T. Chen, "Analytical on-load subdomain field model of permanent-magnet vernier machines," *IEEE Trans. Ind. Electron.*, vol. 63, no. 7, pp. 4105-4117, Jul. 2016.

[5] L. Xu, G. Liu, W. Zhao, X. Yang, and R. Cheng, "Hybrid stator design of fault-tolerant permanent-magnet vernier machines for direct-drive applications," *IEEE Trans. Ind. Electron.*, vol. 64, no. 1, pp. 179-190, Jan. 2017.

[6] J. Du, D. Liang, and X. Liu, "Performance analysis of a mutually coupled linear switched reluctance machine for direct-drive wave energy conversions," *IEEE Trans. Magn.*, vol. 53, no. 9, Art. ID. 8108110, Sep. 2017.

[7] J. Song, J. H. Lee, D. Kim, Y. Kim, and S. Jung, "Analysis and modeling of permanent magnet variable flux memory motors using magnetic equivalent circuit method," *IEEE Trans. Magn.*, vol. PP, no. 99, Art. ID. 8208905, May 2017.

[8] Y. Zhong, L. Wu, X. Huang, Y. Fang, and J. Zhang, "An improved magnetic circuit model of a 3-DOF magnetic bearing considering leakage and cross coupling effects," *IEEE Trans. Magn.*, vol. PP, no. 99, Art. ID. 8002506, May 2017.

[9] P. Naderi and A. Shiri, "Rotor/stator inter-turn short circuit fault detection for saturable wound-rotor induction machine by modified magnetic equivalent circuit approach," *IEEE Trans. Magn.*, vol. PP, no. 99, Art. ID. 8107013, Jul. 2017.

[10] W. Ding, D. Liang, and R. Tang, "A fast nonlinear variable structure equivalent magnetic circuit modeling for dual channel

switched reluctance machine," *Energy Convers. Manage.*, vol. 52, no. 1, pp. 3652-3663, Sep. 2011.
[11] J. Song, J. H. Lee, D. Kim, Y. Kim, and S. Jung, "Analysis and modeling of concentrated winding variable flux memory motor using magnetic equivalent circuit method," *IEEE Trans. Magn*., vol. PP, no. 99, Art. ID. 8102704, Jun. 2017.
[12] E. Severson, R. Nilssen, T. Undeland, and N. Mohan, "Magnetic equivalent circuit modeling of the AC homopolar machine for flywheel energy storage," *IEEE Trans. Energy Convers*, vol. 30, no. 4, pp. 1670-1678. Dec. 2015.
[13] W. Li, K. T. Chau, C. Liu, S. Gao, and D. Wu, "Analysis of tooth-tip flux leakage in surface-mounted permanent magnet linear vernier machine," *IEEE Trans. Magn*., vol. 49, no. 7, pp. 3949-3952, Jul. 2013.
[14] G. Liu, S. Jiang, W. Zhao, and Q. Chen, "A new modeling approach for permanent magnet vernier machine with modulation effect consideration," *IEEE Trans. Magn*., vol. 53, no. 1, pp.1-12, Art. ID. 8100312, Jan. 2017.
[15] H. Chen, W. Yan, and Q. Wang, "Electromagnetic analysis of flux characteristics of double-sided switched reluctance linear machine," *IEEE Trans. Appl. Supercond*., vol. 26, no. 4, pp.1-7, Art. ID. 0603407, Jun. 2016.
[16] J. T. Chen, and Z. Q. Zhu, "Influence of the rotor pole number on optimal parameters in flux-switching PM brushless AC machines by the lumped-parameter magnetic circuit model," *IEEE Trans. Ind. Appl.*, vol. 46, no.4, pp. 1381-1388, Jul. 2010.
[17] T. Hosoi, K. Shima, and T. Fukami, "Magnetic circuit analysis of permanent-magnet-assisted salient-pole synchronous machines under steady states," *IEEE Trans. Ind. Appl.*, vol. 48, no. 3, pp. 895-902, May 2012.
[18] Q. Yu, X. Wang, and Y. Cheng, "Magnetic modeling of saliency effect for saturated electrical machines with a new calculation method," *IEEE Trans. Magn.*, vol. 52, no. 6, pp.1-6, Art. ID. 8001106, 2016.
[19] Q. Chen, G. Liu, W. Zhao, and M. Shao, "Nonlinear adaptive lumped parameter magnetic circuit analysis for spoke-type fault-tolerant permanent-magnet motors," *IEEE Trans. Magn*., vol. 49, no. 9, pp. 5150-5157, Sep. 2013.
[20] S. Ouagued, Y. Amara, and G. Barakat, "Comparison of hybrid analytical modelling and reluctance network modelling for pre-design purposes," *Math. Comput. Simulation*, vol. 130, pp. 3-21, Dec. 2016.
[21] H. Gorginpour, H. Oraee, and R. A. McMahon, "A novel modeling approach for design studies of brushless doubly fed induction generator based on magnetic equivalent circuit," *IEEE Trans. Energy Convers*., vol. 28, no. 4, pp. 902-912, Dec. 2013.

Shan Jiang received the B.Sc. degree in electrical engineering from Jiangsu University, Zhenjiang, China, in 2015. He is currently working toward the M.Sc. degree.

His current research interests include computation of electromagnetic fields for permanent-magnet machine, and electric machine design.

Guohai Liu (M'07–SM'15) received the B.Sc. from Jiangsu University, China, in 1985, and the M.Sc and Ph.D. degrees from Southeast University, China, in 1988 and 2002, respectively, in electrical engineering and control engineering.

Since 1988, he has been with Jiangsu University, where he is currently a Professor, the Dean of the School of Electrical Information Engineering. His teaching and research interests include electrical machines, motor drives for electric vehicles and intelligent control. He has authored or co-authored over 150 technical papers and 4 textbooks, and holds 15 patents in these areas.

Wenxiang Zhao (M'08–SM'14) received the B.Sc. and M.Sc. degrees in electrical engineering from Jiangsu University, Zhenjiang, China, in 1999 and 2003, respectively, and the Ph.D. degree in electrical engineering from Southeast University, Nanjing, China, in 2010.

He has been with Jiangsu University since 2003, where he is currently a Professor with the School of Electrical Information Engineering. From 2008 to 2009, he was a Research Assistant with the Department of Electrical and Electronic Engineering, University of Hong Kong, Hong Kong. From 2013 to 2014, he was a Visiting Professor with the Department of Electronic and Electrical Engineering, University of Sheffield, Sheffield, U.K. His current research interests include electric machine design, modeling, fault analysis, and intelligent control. He has authored and co-authored over 130 technical papers in these areas.

Liang Xu (S'15) received the B.Sc. degree in electrical engineering and automation from Soochow University, Suzhou, China, in 2011, and the M.Sc and Ph.D. degrees from Jiangsu University, Zhenjiang, China, in 2014 and 2017, respectively.

He has been with Jiangsu University since 2017, where he is currently a Lecturer in the School of Electrical Information Engineering. His areas of interest include electrical machines and drives.

Qian Chen (M'16) received the B.Sc. and Ph.D. degrees from Jiangsu University, Zhenjiang, China, in 2009 and 2015, respectively, in electrical engineering and control engineering.

He has been with Jiangsu University since 2015, where he is currently an Associate Professor in the School of Electrical Information Engineering. His current research interests include electric machine design, modeling, fault analysis, and intelligent control.